Asian Journal of Chemistry; Vol. 33, No. 8 (2021), 1783-1790

ASIAN JOURNAL OF CHEMISTRY

https://doi.org/10.14233/ajchem.2021.23242

Influence of Variant Temperatures in Optical, Magnetic Properties of NiO Nanoparticles and its Supercapacitor Applications *via* Precipitation Method

S. SIVAKUMAR* and NAZIR AHMAD MALA

Department of Physics, Annamalai University, Annamalai Nagar-608002, India

*Corresponding author: E-mail: girihari777@yahoo.com

Received: 10 April 2021; *Accepted*: 8 May 2021; *Published online*: 26 July 2021; AJC-20428

In this study, nickel oxide nanoparticles have been synthesized *via* precipitation method and calcinated at 500, 600, 700 and 800 ºC, respectively. TG/DTA curves expose the thermal stability of the prepared/asprepared product. The XRD results revealed that NiO nanoparticles have cubic structure. Crystallite sizes increase with increasing calcination temperatures by using two different methods *via* Scherer′s method and W-H method. The SEM and TEM images confirmed that the NiO nanoparticles have a spherical morphology with high agglomeration. The photoluminescence (PL) and FT-IR spectra give details of the crystal defects and functional groups present in the prepared samples. The energy bandgap of the prepared products was observed to be decreasing (3.59 to 3.01 eV), respectively. The VSM study confirms the occurrence of weak ferromagnetic behaviour. The highest specific capacitance of 555.62 F g^{-1} at 10 mV/s was obtained for NiO (800 ºC) nanoparticles.

Keywords: Precipitation method, NiO nanoparticles, Photoluminescence, Vibrating sample magnetometer, Cyclic voltammetry.

INTRODUCTION

Nano-sized materials have obtained much awareness from the last two decade because of its excellent optical, electronic, chemical, thermal, supercapacitor and magnetic properties. In particular, nano-sized magnetic materials often exhibit superior properties that diverge constantly from those in the bulkiness form [1,2]. Recently, the magnetism of nano-sized materials has taken an imperative role in nanoscience owing to its spectacular properties such as electronics [3], automotive [4], actuators [5], sensor wave absorbers [6], electromagnetic [7], photocatalysis [8], magnetic recording disks [9] and numerous biomedical applications [10]. Transition metal elements are playing a significant role in the field of energy storage devices because of their morphologies and electrochemical behaviour towards the supercapcitor applications.

Supercapacitor is one of the innovative field as they mingle the properties of batteries and capacitors [11,12]. Supercapcitor is an electronic device, which is used to store massive amount of electrical charge, mainly depends up on the electrode material and electrolyte. The selection of the proper electrode with its good electrical conductivity has influenced in the electrochemical performance and price of supercapcitor which makes the production widely spread. There are numerous oxide materials applied for magnetism and supercapacitors including NiS, RuO_2, SnO_2, ZrO_2, NiO, MnO_2, *etc*. Among these, NiO is considered a crucial material because of its demanding many fields and have broad potential applications in numerous fields such as gas sensors [11], fuel cell [13], electro-chromic films [14], battery cathodes [15], recording media [16], photovoltaic devices [17], electrochemical supercapacitors [18], smart windows [19], dye sensitized photo-cathodes [20] and drug delivery [21].

Several methods have been developed to synthesize NiO nanoparticles such as sol-gel [2], micro-emulsion [22], co-precipitation [23], hydrothermal [24], combustion method [25], precipitation method [26] and so on. Among the various methods, precipitation method is usually adopted for the preparation of NiO nanoparticles because it is straight forward and low temperatures synthesis. In this study, NiO nanoparticles have been effectively prepared using precipitation method and the obtained products are calcinated at 500, 600, 700 and 800 ºC. The prepared NiO nanoparticles were utilized for magnetic and supercapcitor applications. The NiO (800 ºC) nanoparticles having spherical morphology and studied as promising working electrode.

EXPERIMENTAL

All the chemicals used in this study were of analytical grade. The principal precursors *viz*. nickel(II) nitrate hexahydrate, citric acid, sodium hydroxide were purchased from Sigma-Aldrich, USA. Double distilled water and acetone were used for all sample preparation and dilutions.

Synthesis: Typically, 0.2 M $Ni(NO_3)_2{\cdot}6H_2O$ and 0.02 M citric acid was dissolved in 50 mL of double distilled water under constant stirring for 30 min. Concurrently, 0.1 M NaOH was dissolved in 50 mL of double distilled water and gradually poured into the homogenous mixture to adjust the pH 12. The sheer solution was gradually changed into green voluminous precipitate. The entire green solution was stirred on a magnetic stirrer at 80 ºC for 1 h. The sample was washed with double distilled water and acetone. The green precipitate sample was dried in a hot air oven at 100 ºC for 6 h and the sample were calcinated in a muffle furnace at 500, 600, 700 and 800 ºC, respectively for 4 h. The calcinated products were milled into finer powders using an agate mortar and pestle and the powder formed was characterized with different techniques.

Instrumentation: The prepared sample were examined by TG/DTA *via* Perkin-Elmer Diamond (NETZ-SCH-STA-449F3) instrument with heating time of 20 ºC/min. The crystallite size and phase identification of the NiO nanoparticles were recorded by an X'PERT-PRO diffractometer with CuKα radiation (λ = 1.5406 Å), operating at a voltage of 40 kV with an applied current of 30 mA. The optical properties of bare NiO nanoparticles were analyzed using Shimadzu-3600 spectrophotometer with BaSO4 as normal reference. The photoluminescence (PL) emission spectrum was observed by Job in-YV-ON, FLUORO-LOG-FL3-11 instrument and using 150 W xenon lamps. The chemical composition and functional groups of the NiO nanoparticles were investigate by FTIR spectroscopy using a Perkin-Elmer spectrometer (spectrum-1000). The chemical composition and morphology of the achieved products were examined by EVO18 MODEL using SEM and EDX, operated at a voltage of 20 kV. The micrographs and particle size of the obtained products were measured using the TEM (JEOL 3010) instrument. The magnetic properties of the products were carried out through the VSM, model-7410.

Electrochemical performance: Thes electrochemical performance of Bare NiO nanoparticles were examined by the electrochemical analyzer. There are three-electrode systems with Ag/AgCl as a reference electrode, platinum foil as a counter electrode and NiO nanoparticles as a working electrode. The measurements are recorded in 2 M aqueous solution of sodium sulfate as an electrolyte. The electrochemical performance was evaluated by using cyclic voltammetry within the 0.0 to 0.6 V *versus* Ag/AgCl potential range at a scanning rate from 10 to 100 mV s^{-1} on the versa STAT-MC Princeton Applied Research electrochemical work station.

RESULTS AND DISCUSSION

Thermal analysis: The thermal stability behaviour of the as-prepared sample was investigated by TG/DTA technique. The TG curve (blue) revealed the three weight loss and corresponding to the DTA (red) curve, which exhibits two weak endothermic peaks (Fig. 1). The first gradual weight loss (5.9 wt %) in the temperatures range at 72-100 ºC owed to the evaporation of water molecule in the outer and inner surface of the sample associated with a weak endothermic peak at 105 ºC in the DTA curve [27]. The second straight weight loss (16.5 wt.%) in the temperature range of 125-300 ºC is due to the disintegration of some organic solvent associated with a second weak endothermic peak at 325 ºC in the DTA curve [28].

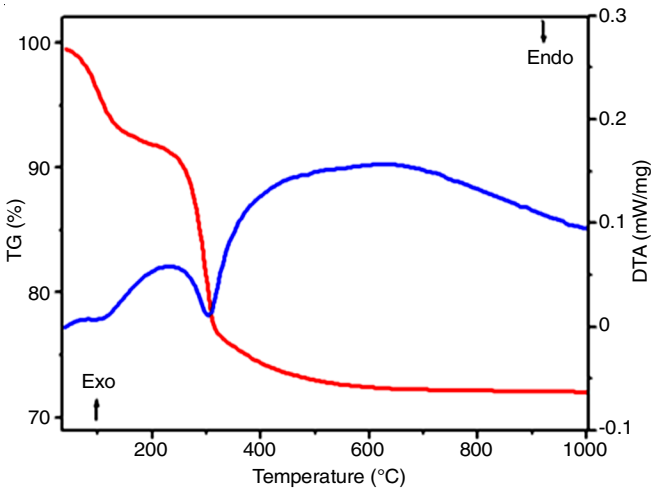

Fig. 1. TG/DTA curve of precurser $Ni(OH)_2$

In continuation, the third weight loss (3.9 wt.%) materialize in the temperature range of 320-400 ºC can be attributed to the disintegration of nickel hydroxide [$Ni(OH)_2$] group [29]. When the calcinations temperature is above 500 ºC no weight loss occur becomes TG curve comparatively in a straight line which signifying the structure of NiO nanoparticles.

X-ray diffraction studies: Fig. 2a displays the XRD peaks of prepared and NiO (500, 600, 700 and 800 ºC) nanoparticles. There is no characteristic diffraction peak, which indicates that the structures of the prepared products are amorphous in nature. The results are in agreement with literature reports [2].

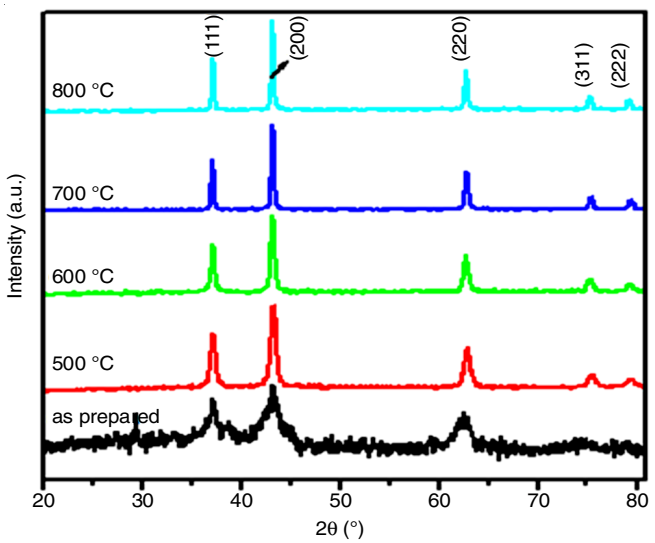

Fig. 2(a). X-ray diffraction pattern of prepared and NiO NPs

The characteristic diffraction peaks are at 37.20º, 43.20º, 62.87º, 75.20º and 79.38º can be indexed as (111), (200), (220), (311), and (222) planes and corresponds to the cubic structure of NiO nanoparticles (JCPDS card No.: 73-1523). In prepared sample (without calcination) shows more impurities and crystal defects, after increasing the calcination temperatures the impurities will be reduced and peaks showed in well crystalline in nature. The crystallite size increases owing to the increasing of calcination temperatures and peaks become sharp as compare to the prepared sample, it was happened due to increase in crystallite size. One more thing, the two peaks (75.20º and 79.38º) were disappeared in prepared sample after increasing the temperatures the peaks are easily identified in the prepared sample (Fig. 2a) and are well coordinated with standard JCPDS card no. 73-1523. The average crystallite size of NiO nanoparticles was calculated by using Scherer's equation [24]:

$$D = \frac{k\lambda}{\beta\cos\theta} \quad (1)$$

The microstrain (ε) is determined by using eqn. 2:

$$\varepsilon = \frac{\beta\cos\theta}{4} \quad (2)$$

The dislocation density (δ) is calculated by using eqn. 3:

$$\delta = \frac{1}{D^2} \quad (3)$$

The lattice parameters (a=b=c) for the cubic phase are determined by using eqn. 4:

$$d = \frac{a}{\sqrt{h^2 + k^2 + l^2}} \quad (4)$$

The volume of the cell is calculated by by using eqn. 5 [30]:

$$V = a^3 \quad (5)$$

where D is the crystallite size, k = 0.9 is the fixed number, λ is the wavelength of X-ray (Cu*K*α = 0.15405 nm), β is the full width half maximum, θ is Bragg's angle and a is the lattice parameter. All the microstructural parameter values are listed in Table-1. The crystallite size increases with increasing the different calcinations temperatures. Correspondingly, the dislocation density and micro-strain shows a decreasing trend with increasing the calcinations temperatures. The lattice parameter and cell volume shows increasing order.

The average crystallite size and lattice strain were computed by Williamson-Hall (W-H) equation (eqn. 6) [31]:

$$\beta\cos\theta = \frac{k\lambda}{D\cos\theta} + 4\varepsilon\sin\theta \quad (6)$$

From eqn. 6, plot is drawn between 4sin θ along *x*-axis *versus* βcos θ along *y*-axis as shown in Fig.2b. The average crystallite size using W-H method is similar to to 21.97, 23.18, 26.01, 26.81 and 27.18 nm for the prepared samples calcined at 500, 600, 700 and 800 ºC, respectively. The calculated values of average crstallite size and microstrain are in close agreement with the values calculated from Scherrer's equation.

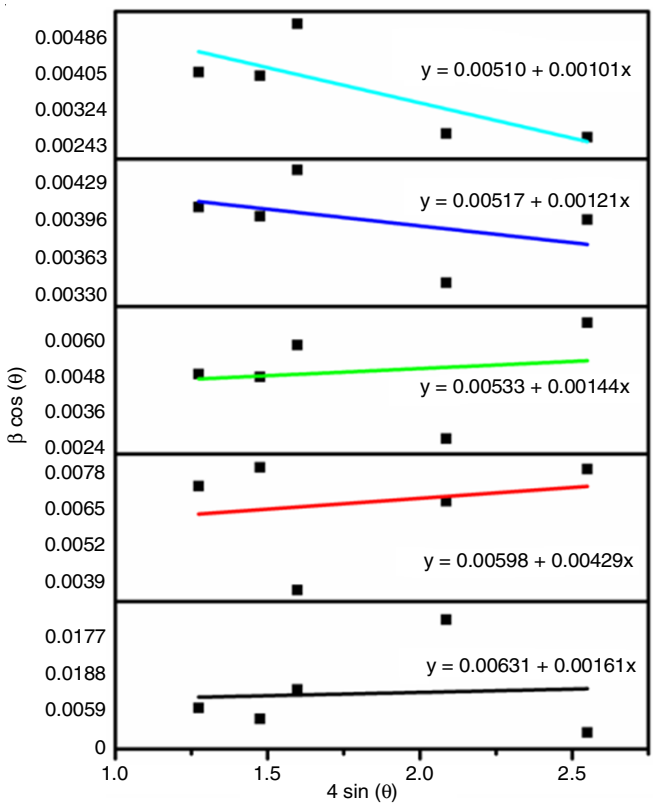

Fig. 2(b). Williamson-Hall plots for prepared and NiO (500, 600, 700 and 800 °C) NPs

FT-IR studies: Fig. 3 shows the FT-IR spectra of prepared and calcinated NiO nanoparticles. The FT-IR peaks of all samples show broad but a slight weak absorption peaks at 3431, 2924, 1633, 1385, 1056, 618 and 482 cm^{-1}, respectively. The broad peak at 3431 cm^{-1} can be assigned to the O–H stretching and a weak peak at 1633 cm^{-1} is attributed to the H–O–H bending vibrations owing to the interlayer water molecules [24,25]. The weak peak at 2924 cm^{-1} is attributed to the C-H symmetric

TABLE-1
STRUCTURAL PARAMETERS OF NiO NANOPARTICLES

Materials	Scherrer method		W-H method		Dislocation density (δ) × 10^{15} L/m^2	Lattice parameter (a = b = c)	Cell volume $V = a^3$	E_g (eV)
	Average (D) (nm)	Micro-strain × 10^3 (ε)	Average (D) (nm)	Lattice strain				
Prepared	18.57	2.3815	21.97	0.00161	2.8998	4.1788	72.97	3.59
500 °C	18.98	1.6678	23.18	0.00429	2.7759	4.1810	73.08	3.25
600 °C	23.70	1.1838	26.01	0.00144	1.7803	4.1826	73.17	3.15
700 °C	26.28	0.9822	26.81	0.00121	1.4479	4.1841	73.24	3.06
800 °C	28.06	0.9452	27.18	0.00101	1.2700	4.1865	73.37	3.01

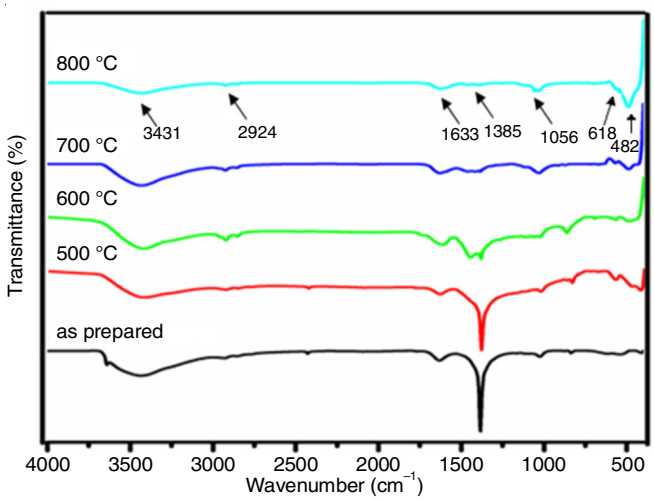

Fig. 3. FT-IR spectra of prepared NiO nanoparticles

stretching mode, while the slightly sharp and weak peaks occurred at 1385 and 1056 cm^{-1} are ascribed to the NO_3^- ions [1]. In addition, the weak absorption peak at 618 cm^{-1} can be allocated to Ni–O–H bending vibrations owing to the creation of nickel hydroxide band. The peak at 482 cm^{-1} can be ascribed to the stretching mode of Ni–O bond. The peak location of the stretching mode of Ni–O band confirms the creation of NiO nanoparticles [20,24]. When increase the calcination temperature, the peaks are reduced it may be owing to the evaporation of solvent/impurities.

UV-DRS studies: The absorption peaks of NiO nanoparticles calcinated at 500, 600, 700 and 800 ºC are shown in Fig. 4. The strong broad absorption edges could be found in the wavelength range of 220-340 nm, which confirms the better optical quality in the UV region. The absorption edge is slightly shifted towards lower wavelength (blue shift) when compared to the prepared products due to thermal effects. The shift in weak peak at 800 ºC for might be due to surface defects present in the material. The energy band gap of the prepared and NiO (500, 600, 700 and 800 ºC) nanoparticles were calculated using eqn. 7 [32]:

$$\alpha = \frac{\sqrt{A(h\nu - E_g)}}{h\nu} \quad (7)$$

where E_g, A and α represent energy gap, proportionality constant and absorption coefficient, respectively. The band gap of the prepared and NiO nanoparticles samples was measured by plotting of $(F(R)h\nu)^2$ *versus* energy (hν). Energy bandgap of the prepared and NiO nanoparticles (500, 600, 700 and 800 ºC) were found to be 3.59, 3.25, 3.15, 3.06 and 3.01 eV, respectively. Previous literature reports on the variable synthesis process of the energy bandgap and crystallite size are listed in Table-2.

TABLE-2
THE BANDGAP ENERGY VALUES REPORTED IN THE LITERATURE

Method	Size (nm)	E_g (eV)	Ref.
Precipitation	17-28	3.01-3.59	Present work
Thermal treatment	14-34	3.51-3.62	[33]
Combustion	28	3.76	[25]
Sol-gel	11-38	3.46-3.87	[34]

Photoluminescence studies: The photoluminescence emission spectrum of the NiO nanoparticles with different calcinations were recorded at 280 nm of excited wavelength as revealed in Fig. 5. The samples show slight sharp but weak NBE (near band edge) UV emission peaks at 343, 377, 401 and 408 nm and two strong broad and slight weaker DL (deep level) visible emission peaks at 425 and 452 nm, respectively. An emission peak was seen at 377 nm, which may be owed to an ionized oxygen vacancy. A weak UV emission can be owing to the NBE of NiO nanoparticles due to the availability of the free electron-holes pair transition [24]. The other strong broad emission peak was observed at 425 nm (blue emission) which might be ascribed to the occurrence of dissimilar defect states in NiO lattice, such as Ni interstitials and oxygen vacancies [1]. When the calcination temperatures increase, the peak intensity showing decreasing. The PL emission values (~377 and 425 nm) are closely associated with the reported values [32,35].

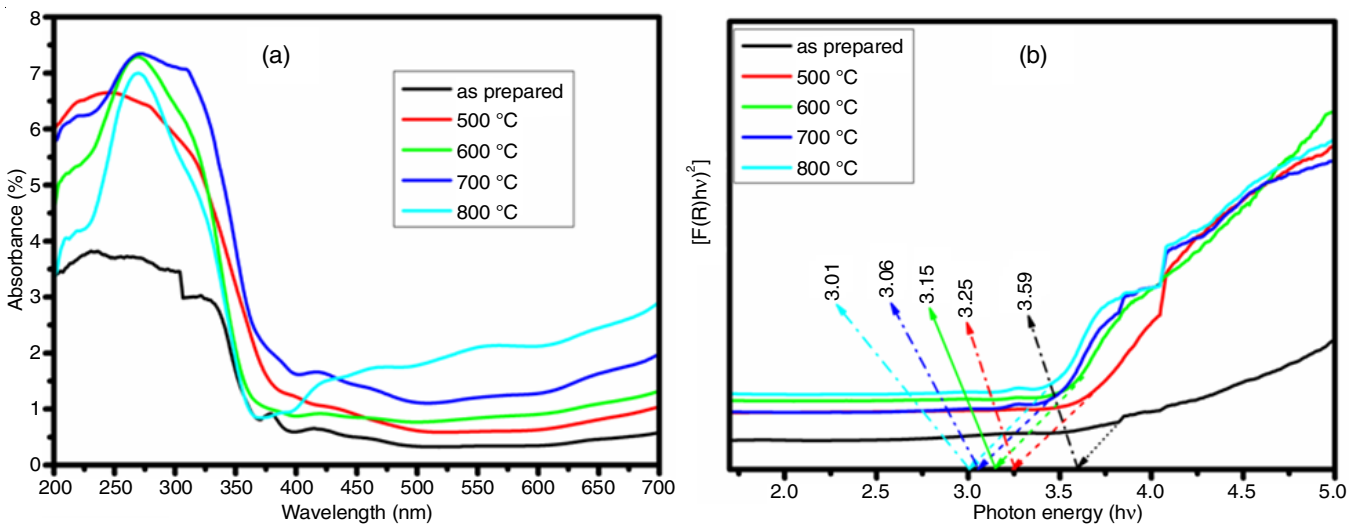

Fig. 4. (a) UV-Visible absorption spectrum and (b) energy bandgap of prepared and NiO nanoparticles

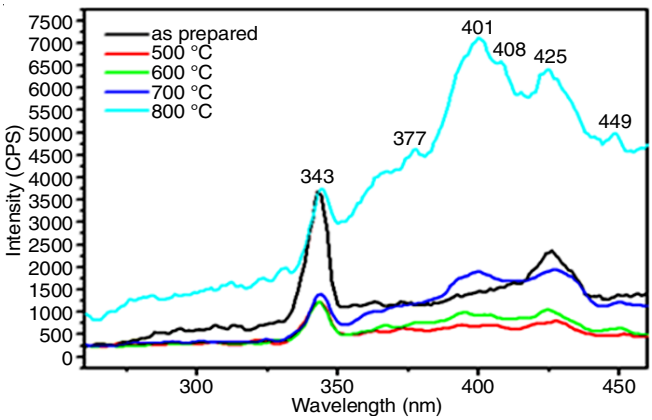

Fig. 5. Photoluminescence (PL) emission spectra of prepared and NiO nanoparticles

SEM/EDX analysis: Fig. 6a-d shows the SEM images of NiO (800 ºC) nanoparticles, which are spherical in shape with high agglomeration. The agglomeration could be mainly due to the owing to the strong chemical bonds adopted, strong surface energy and small dimensions. The elemental composition of NiO (800 ºC) nanoparticles was performed using EDX analysis. The peak signal of two elements namely Nickel (Ni) and oxygen (O) was determined in the EDX spectra of the NiO (800 ºC) nanoparticles (Fig. 6e). It confirms the creation of NiO nanoparticles. The mass and atomic mass percentage of Ni and O in the current product are shown in Fig. 6e, and the obtained results do not reflect any unwanted secondary peak corresponding to any impurity element as shown in Fig. 6e. This is excellent apparent with XRD results.

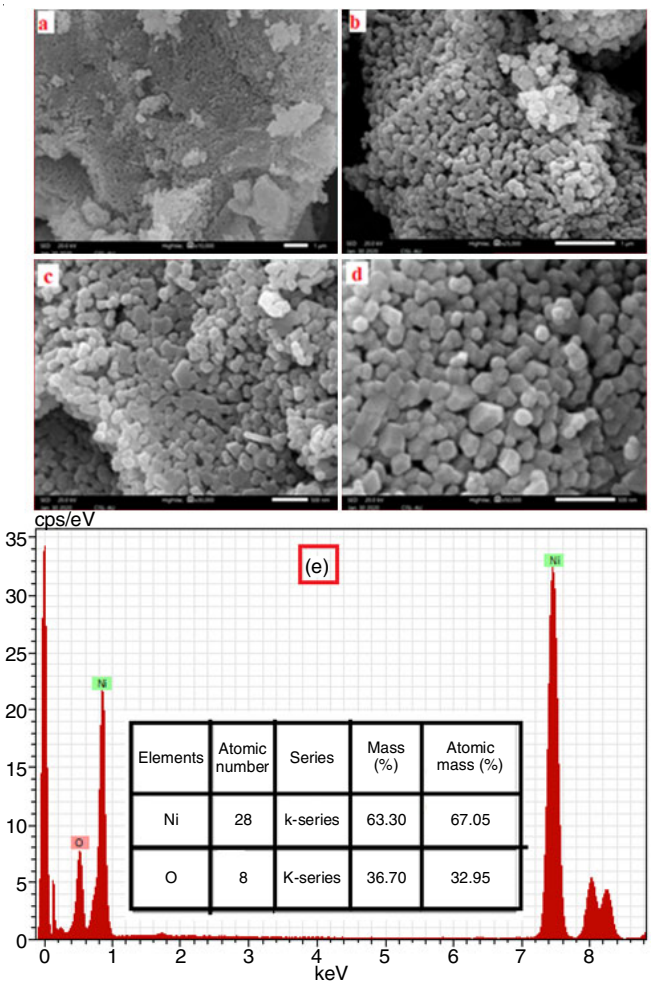

Fig. 6. (a-d) SEM images and 6(e) EDX spectrum of bare NiO (800 °C)

TEM/SAED analysis: The TEM and SAED patterns of the NiO nanoparticles (800 ºC) are shown in Fig. 7a-e. It was observed that most of the particles are spherical in shape with agglomeration, which is already confirmed by SEM result. Fig. 7c shows HR-TEM image, which indicates the occasion of lattice planes with an interplaner spacing of 0.24 nm and related to (200) plane of the FCC structure of NiO nanoparticles, which is good agreement with the XRD results. The SAED patterns of NiO (800 ºC) nanoparticles exhibit bright polycrystalline spots (800 ºC). The average crystallite size of NiO (800 ºC) nanoparticles was calculated by using J-image software and found to be around 19 nm.

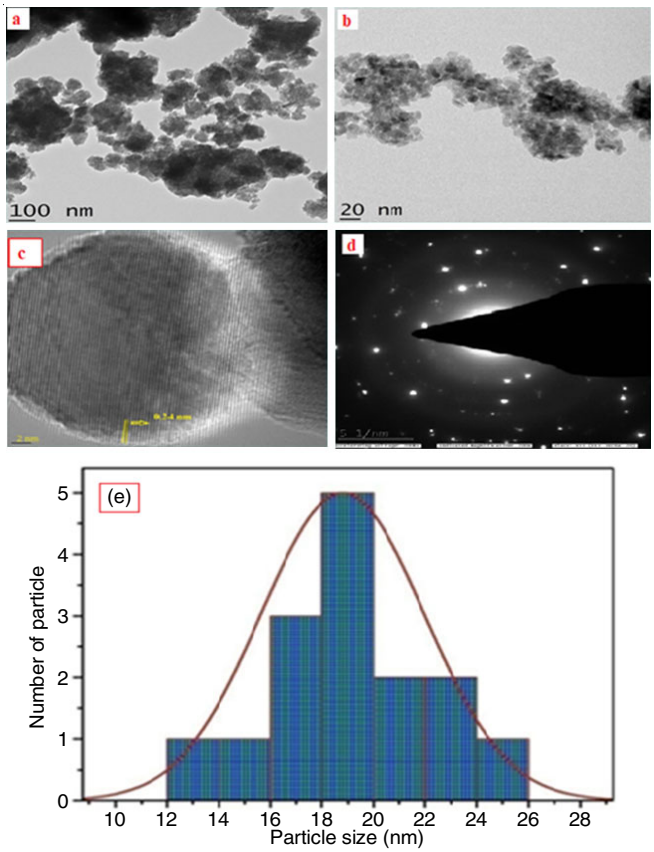

Fig. 7. (a-c) TEM images, (d) SAED image, (e) Histogram image of NiO (800 °C) nanoparticles

Magnetic studies: Fig. 8a shows magnetic hysteresis measurements of the prepared and NiO nanoparticles at 500, 600, 700 and 800 ºC. The M-H measurement of the prepared samples shows weak ferromagnetic behaviour at room temperature (T_r). The origin of the ferromagnetic possessions can be attributed due to the bare NiO nanoparticles on the size confinement effect. Bare NiO nanoparticles were composed up of tiny magnetic domains, each of which is characterized and randomly oriented by its magnetic moment. The sum of such magnetic domains coupled with dipolar interactions is the total magnetic moment of the nanoparticles. The values of

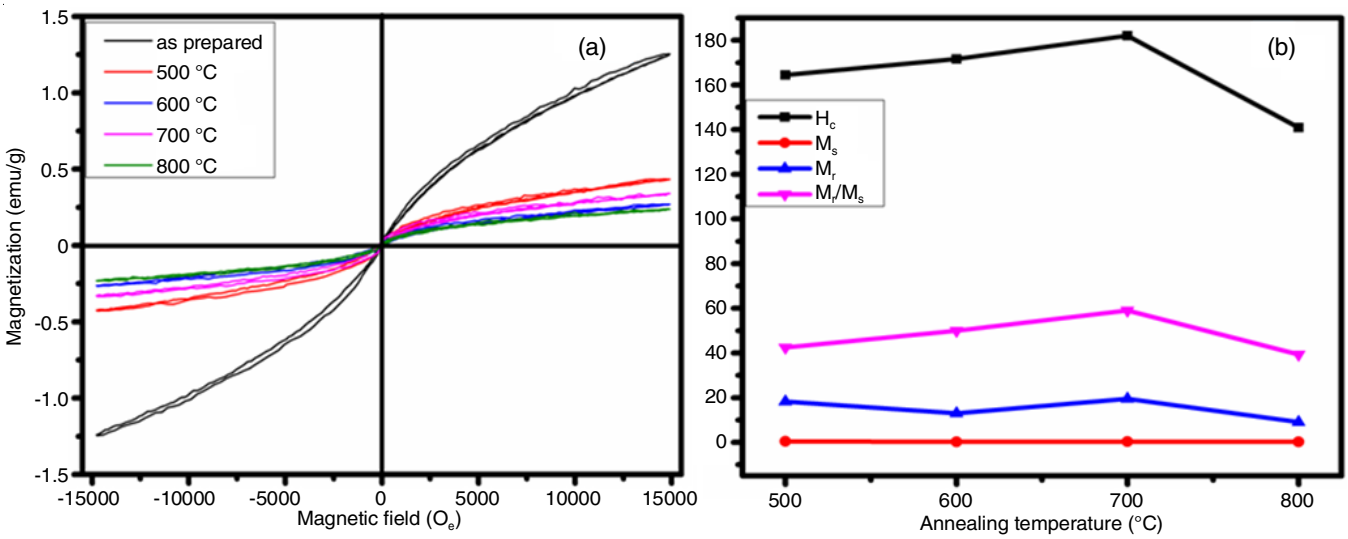

Fig. 8. (a) M-H curves of prepared, 500, 600, 700 and 800 °C. (b) shows curves of H_c, M_r, M_s, M_r/M_s and annealing temperature

coercivity (H_c), saturation magnetization (M_s) and remanence (M_r) for the prepared NiO nanoparticles at 500, 600, 700 and 800 ºC are tabulated in Table-3.

TABLE-3
MAGNETIC PARAMETERS OF PREPARED AND NiO NPs

Temp. (°C)	VSM of Hysteresis parameters			SQR = M_r/M_s
	H_c (Oe)	M_s (emu/g)	$M_r \times 10^{-3}$ emu/g	SQR × 10^{-3}
Prepared	33.24	1.24	20.18	16.27
500	164.42	0.43	18.26	42.46
600	171.68	0.26	13.00	50.00
700	182.05	0.33	19.49	59.06
800	140.93	0.23	0.905	3.93

In general, the magnetic behaviour of NiO nanoparticles are antiferromagnetic when it is bulk form, after reduced its size in nanoscale then exhibit magnetic behaviour owing to the amount of ferromagnetic Ni segment and surface magnetization. As obviously seen in Fig. 8a, the magnetization of NiO nanoparticles increases linearly with increasing magnetic fields and does not achieve a saturation value up to the maximum field applied in the VSM analysis [1]. In NiO structure, there are straight atomic chains of nickel-oxygen-nickel with dominating exchange interactions and inverse spins along the (111) direction. When applied the magnetic field no response will occur may be due to the compensated spins. In between the two neighbouring nickel divalent ions, the super-exchange interaction in NiO structure occur due to mediated by an oxygen ions. It is pointed out that the exchange is responsive to bond angles and bond lengths. As a result, when oxygen ion is disturbed the size of the bulk NiO reduced to the nanoscale and the bond covalence is broken to induce its surface spin disorder. The faction of atoms residing on the particles surface increases as the particle size decreases, so the surface spin disorder and uncompensated surface spins increase [36]. Dissimilar magnetic behaviours, such as super-paramagnetism (crystallite size $D \leq 32$ nm), ferromagnetism ($D \leq 24$ nm) and spin glass ($D \leq 10$ nm) behaviour can be exhibited in the NiO material when the particle sizes are reduced to the nanometer range [1]. Therefore, the magnetic properties correlate to structural behaviour especially crystallinity, shape, size, strain and so on. This result is in good agreement with previous reports [37,38].

Electrochemical studies: Fig. 9 depicts the cyclic voltammogram of the prepared and NiO nanoparticles at 500, 600, 700 and 800 ºC. The cyclic voltammograms of all the samples show redox peaks, which demonstrated that the capacitance characteristic has completely deviated from that of the electric double-layer capacitor (EDLC). The occurrence of redox peaks denotes a pseudocapacitive behaviour of the products, which develops the reversible electrochemical reactions. The main advantage for pseudocapacitance relates to its high energy transport through the Faradaic process and supplying 10-100 times

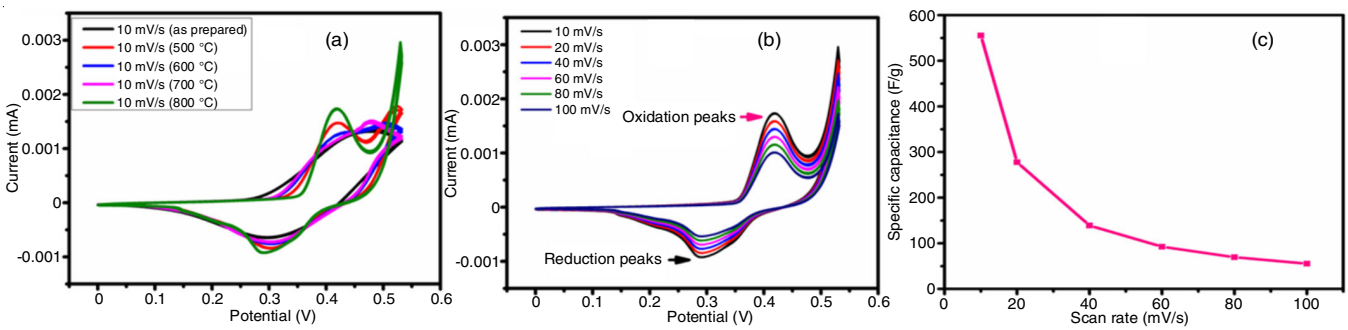

Fig. 9. (a) CV curves of NiO naoparticles at 10 mV/s, (b,c) CV curves and C_s values of NiO (800 °C) at different scan rates

extra capacitance than EDLC [39]. The probable reversible chemical reaction could be caused by the intercalation/de-intercalation of sodium sulfate into/from the NiO lattice.

$$NiO + Na_2SO_4 + e^- \rightleftharpoons (NiO)\,Na_2SO_4$$

The Faradaic reactions of NiOOH can be expressed as follows:

$$Ni(OH)_2 + OH^- \rightleftharpoons NiOOH + H_2O + e^-$$

$$Ni(OH)_2 \rightleftharpoons NiO + H_2O$$

The specific capacitance (C_s) of all the electrodes was calculated from the CV curves using eqn. 8:

$$C_s = \frac{Q}{m\Delta V} \quad (8)$$

where Q is the cathodic and anodic charges on each scanning, ΔV is the scan rate (mV/s) and m is the mass of the active material (mg) in the electrode.

Applying eqn. 8, the specific capacitance (C_s) of all the products were calculated at 10 mV s^{-1} were 147.53, 191.92, 237.44, 373.80 and 555.62 F g^{-1}. It is evident that bare NiO (800 ºC) electrode has shown the highest C_s value, which maybe due to low energy bandgap and spherical morrphology in the samples. Further at different scan rates have been done particular at 800 ºC and different C_s values are 555.62, 277.81, 138.90, 92.60, 69.45 and 55.56 F g^{-1} for various scan rates 10, 20, 40, 60, 80 and 100 mV s^{-1}, respectively. The increasing movement of specific capacitance on the NiO electrode with increasing different temperatures. In the current study, the specific capacitance is high at a low scan rate, which could be resulted from the low Faradaic reaction. At low scan rate, both inside and outside surfaces depend on the calibration of specific capacitance, which gives the superior value of specific capacitance. At high scan rates, the ionic diffusion occurs from the surfaces of outside region. The specific capacitance maintains the charge at 55.56 F g^{-1} at the scan rate 100 mV s^{-1}.

Conclusion

In summary, nickel oxide nanoparticles have been synthesized by precipitation method. The XRD confirmed that the dislocation density,while the micro-strain shows a decreasing trend with increasing the calcinations temperatures. The NiO nanoparticles calcinated at higher temperatures (500-800 ºC) showed a shift towards the lower wavelength region (blue-shift) when compared to that of the prepared sample. The SEM and TEM images showed the spherical particles with size of 19 nm. The magnetic studies showed the existence of weak ferr-magnetic character, which can be used for soft magnetic materials. The cyclic measurements were investigated at four different calcination temperatures, among the studied temperature 800 ºC shows the promising NiO electrode material characteristics.

CONFLICT OF INTEREST

The authors declare that there is no conflict of interests regarding the publication of this article.

REFERENCES

1. R. Suresh, V. Ponnuswamy, C. Sankar, M. Manickam, S. Venkatesan and S. Perumal, *J. Magn. Magn. Mater.*, **441**, 787 (2017); https://doi.org/10.1016/j.jmmm.2017.05.069
2. M. Alagiri, S. Ponnusamy and C. Muthamizhchelvan, *J. Mater. Sci. Mater. Electron.*, **23**, 728 (2012); https://doi.org/10.1007/s10854-011-0479-6
3. K.M. Krishnan, A.B. Pakhomov, Y. Bao, P. Blomqvist, M. Gonzales, Y. Chun, K. Griffin, X. Ji and B.K. Roberts, *J. Mater. Sci.*, **41**, 793 (2006); https://doi.org/10.1007/s10853-006-6564-1
4. N.M. Deraz, *J. Alloys Compd.*, **501**, 317 (2010); https://doi.org/10.1016/j.jallcom.2010.04.096
5. M. Pita, J.M. Abad, C. Vaz-Dominguez, C. Briones, E. Mateo-Martí, J.A. Martín-Gago, M. del Puerto Morales and V.M. Fernández, *J. Colloid Interface Sci.*, **321**, 484 (2008); https://doi.org/10.1016/j.jcis.2008.02.010
6. G. Balaji, R.A. Narayanan, A. Weber, F. Mohammad and C.S.S.R. Kumar, *Mater. Sci. Eng. B*, **177**, 14 (2012); https://doi.org/10.1016/j.mseb.2011.09.023
7. H. Wu, M. Qin and L. Zhang, *Composite B*, **182**, 107620 (2019); https://doi.org/10.1016/j.compositesb.2019.107620
8. J. Lin, J. Shen, T. Wang, R. Wang, H. Liu, J. Cui and W. Zhou, *Mater. Sci. Eng. B*, **176**, 921 (2011); https://doi.org/10.1016/j.mseb.2011.05.018
9. N.M. Deraz and A. Alarifi, *J. Anal. Appl. Pyrolysis*, **97**, 55 (2012); https://doi.org/10.1016/j.jaap.2012.04.006
10. D. Chen, H. Liu and L. Li, *Mater. Chem. Phys.*, **134**, 921 (2012); https://doi.org/10.1016/j.matchemphys.2012.03.091
11. R. Kötz and M.J.E.A. Carlen, *Electrochim. Acta*, **45**, 2483 (2000); https://doi.org/10.1016/S0013-4686(00)00354-6
12. B. Ksapabutr, P. Nimnuan and M. Panapoy, *Mater. Lett.*, **153**, 24 (2015); https://doi.org/10.1016/j.matlet.2015.03.151
13. R.C. Makkus, K. Hemmes and J.H.W. de Wit, *J. Electrochem. Soc.*, **141**, 3429 (1994); https://doi.org/10.1149/1.2059349
14. Z. Jiao, M. Wu, Z. Qin and H. Xu, *Nanotechnology*, **14**, 458 (2003); https://doi.org/10.1088/0957-4484/14/4/310
15. F. Zheng, S. Xu and Y. Zhang, *J. Mater. Sci. Mater. Electron.*, **27**, 3576 (2016); https://doi.org/10.1007/s10854-015-4194-6
16. S. Morup and A. Hernando, Studies of Superparamagnetism in Samples of Ultrafine Particles, Nanomagnetism, Kluwer Academic Publishers: Boston, USA, pp 93-99 (1993).
17. M. Borgstrom, E. Blart, G. Boschloo, E. Mukhtar, L. Hammarstrom, A. Hagfeldt and F. Odobel, *J. Phys. Chem. B*, **109**, 22928 (2005); https://doi.org/10.1021/jp054034a
18. K.-C. Liu and M.A. Anderson, *J. Electrochem. Soc.*, **143**, 124 (1996); https://doi.org/10.1149/1.1836396
19. C.G. Granqvist, Handbook of Inorganic Electrochromic Materials, Elsevier: Amsterdam (1995).
20. B. Govindarajan, R. Palanimuthu and K.M. Manikandan, *J. Mater. Sci. Mater. Electron.*, **30**, 6519 (2019); https://doi.org/10.1007/s10854-019-00957-2
21. J.W. Rasmussen, E. Martinez, P. Louka and D.G. Wingett, *Expert Opin. Drug Deliv.*, **7**, 1063 (2010); https://doi.org/10.1517/17425247.2010.502560
22. D.Y. Han, H.Y. Yang, C.B. Shen, X. Zhou and F.H. Wang, *Powder Technol.*, **147**, 113 (2004); https://doi.org/10.1016/j.powtec.2004.09.024
23. K. Karthik, G.K. Selvan, M. Kanagaraj, S. Arumugam and N.V. Jaya, *J. Alloys Compd.*, **509**, 181 (2011); https://doi.org/10.1016/j.jallcom.2010.09.033
24. R.S. Kumar, S.J. Jeyakumar, M. Jothibas, I.K. Punithavathy and J.P. Richard, *J. Mater. Sci. Mater. Electron.*, **28**, 15668 (2017); https://doi.org/10.1007/s10854-017-7456-7
25. S.B. Patil, T.N. Ravishankar, K. Lingaraju, G.K. Raghu and G. Nagaraju, *J. Mater. Sci. Mater. Electron.*, **29**, 277 (2018); https://doi.org/10.1007/s10854-017-7914-2

26. S. Sivakumar, E. Manikandan, B. Mahalakshmi, N.A. Mala and L.N. Prabu, *Vacuum*, **173**, 109116 (2020); https://doi.org/10.1016/j.vacuum.2019.109116
27. C.V. Reddy, C. Byon, B. Narendra, D. Baskar, G. Srinivas, J. Shim and S.V. Prabhakar Vattikuti, *Superlatt. Microstruct.*, **82**, 165 (2015); https://doi.org/10.1016/j.spmi.2015.02.014
28. K. Kaviyarasu, E. Manikandan, J. Kennedy, M. Jayachandran, U.U. De Gomes, R. Ladchumananandasiivam and M. Maaza, *Ceram. Int.*, **42**, 8385 (2016); https://doi.org/10.1016/j.ceramint.2016.02.054
29. A. Barakat, M. Al-Noaimi, M. Suleiman, A. Aldwayyan, B. Hammouti, T. Hadda, S. Haddad, A. Boshaala and I. Warad, *Int. J. Mol. Sci.*, **14**, 23941 (2013); https://doi.org/10.3390/ijms141223941
30. K.M. Batoo, E.H. Raslan, Y. Yang, S.F. Adil, M. Khan, A. Imran and Y. Al-Douri, *AIP Adv.*, **9**, 055202 (2019); https://doi.org/10.1063/1.5078411
31. Z.N. Kayani, A. Kamran, Z. Saddiqe, S. Riaz and S. Naseem, *J. Photochem. Photobiol. B*, **183**, 357 (2018); https://doi.org/10.1016/j.jphotobiol.2018.04.051
32. G. Rajesh, S. Akilandeswari, D. Govindarajan and K. Thirumalai, *Mater. Res. Express*, **6**, 1050a9 (2019); https://doi.org/10.1088/2053-1591/ab405e
33. M. Hashem, E. Saion, N.M. Al-Hada, H.M. Kamari, A.H. Shaari, Z.A. Talib, S.B. Paiman and M.A. Kamarudeen, *Results Phys.*, **6**, 1024 (2016); https://doi.org/10.1016/j.rinp.2016.11.031
34. S.R. Nalage, M.A. Chougule, S. Sen, P.B. Joshi and V.B. Patil, *Thin Solid Films*, **520**, 4835 (2012); https://doi.org/10.1016/j.tsf.2012.02.072
35. B. Kisan, P. Saravanan, S. Layek, H. Verma, D. Hesp, S. Krishnamurthy, V. Dhanak and A. Perumal, *J. Magn. Magn. Mater.*, **384**, 296 (2015); https://doi.org/10.1016/j.jmmm.2015.02.065
36. A. Jafari, S.P. Jahromi, K. Boustani, B.T. Goh and N.M. Huang, *J. Magn. Magn. Mater.*, **469**, 383 (2019); https://doi.org/10.1016/j.jmmm.2018.08.005
37. A.A. Ezhilarasi, J.J. Vijaya, K. Kaviyarasu, R.J. Ramalingam, L.J. Kennedy and H.A. Al-Lohedan, *J. Photochem. Photobiol. B*, **180**, 39 (2018); https://doi.org/10.1016/j.jphotobiol.2018.01.023
38. F. Motahari, M.R. Mozdianfard, F. Soofivand and M. Salavati-Niasari, *RSC Adv.*, **4**, 27654 (2014); https://doi.org/10.1039/c4ra02697g
39. K. Sathishkumar, N. Shanmugam, N. Kannadasan, S. Cholan and G. Viruthagiri, *Mater. Sci. Semicond. Process.*, **27**, 846 (2014); https://doi.org/10.1016/j.mssp.2014.08.025